



Suppressed dielectric loss and enhanced breakdown strength in Ni/PVDF composites through constructing Al₂O₃ shell as an interlayer

Guozheng Cao¹, Wenyong Zhou^{1,*} , Yuyao Li¹, Peiqi Liu¹, Tian Yao¹, Jin Li¹,
Jing Zuo¹, Jiangtao Cai¹, and Ying Li^{2,*}

¹School of Chemistry and Chemical Engineering, Xi'an University of Science & Technology, Xi'an 710054, China

²School of Materials Science and Engineering, Xi'an University of Science & Technology, Xi'an 710054, China

Received: 9 December 2021

Accepted: 24 February 2022

Published online:

9 March 2022

© The Author(s), under exclusive licence to Springer Science+Business Media, LLC, part of Springer Nature 2022

ABSTRACT

Developing polymer dielectrics with a low dielectric loss but high dielectric permittivity (ϵ') and breakdown strength (E_b) is constantly pursued for applications in microelectronics and electrical industries. In this work, nickel (Ni) powders were coated by a layer of insulating aluminum oxide (Al₂O₃) via a facile sol–gel process, and the obtained core–shell Ni@Al₂O₃ particles were admixed into poly(vinylidene fluoride) (PVDF) to study the impacts of the Al₂O₃ shell and its thickness on dielectric properties of the composites. The results verify the formation of the insulating Al₂O₃ layer on the surface of the Ni core, which obviously enhances interfacial compatibility and interactions between the matrix and the fillers. The Ni@Al₂O₃/PVDF composites show better dielectric performances compared with the pristine Ni/PVDF. The dramatically suppressed dielectric loss and conductivity can be attributed to the insulating Al₂O₃ interlayer avoiding the Ni cores from direct contact with each other and blocking the long-range migration of electrons. Furthermore, the Al₂O₃ shell serves as an interlayer which lessens the distortion and concentration of local electric field subsequently leading to enhanced E_b . Thus, the dielectric properties of the Ni@Al₂O₃/PVDF composites can be effectively tuned through finely tailoring the Al₂O₃ shell's thickness. The developed Ni@Al₂O₃/PVDF composites with high E_b and ϵ' but low dielectric loss have potential applications in the microelectronic and electrical industries.

Address correspondence to E-mail: wyzhou2004@163.com; liyingxust@126.com

1 Introduction

In the past few years, with the rapid development of the microelectronics industry, dielectric materials with high dielectric constant (ϵ') and low dielectric loss have been favored by researchers because of their wider practical engineering applications (e.g., energy storage devices, microelectronics, kinetic weapons, power converters, etc.) [1–8]. Traditional inorganic ferroelectric ceramic materials like BaTiO₃ [9], Pb(Zr_{0.25}Ti_{0.84})O₃ (PZT) [10], Ba(Zr_{0.3}Ti_{0.7})O₃ (BZT) [11], CaCu₃Ti₄O₁₂ [12] and SrTiO₃ [13], etc., exhibit rather high ϵ' as well as good thermal stability. However, they cannot meet the rigorous requirements for advanced electronic devices owing to their large dielectric loss and high sintering temperature, inherent brittleness as well as high production cost [14, 15]. Compared to widely used ceramic materials, polymers have the prominent advantages like very low dielectric loss, high breakdown strength (E_b), ease of processing, lightweight, and low cost [16–19]. However, the presence of the low ϵ' significantly limits their practical engineering applications. Therefore, neither single ceramic materials nor polymers solely can satisfy the rigid requirements for the fast-developing microelectronics industry [20–22]. Hence, in order to achieve both high ϵ' and low loss, polymer composites reinforced with ceramic or conductive particles as fillers have been introduced and attracted wide attention owing to the combined physical properties from each component.

Generally, there are two strategies to enhance ϵ' of polymers, i.e., either using ceramics or conductive particles as functional fillers. Ceramic particles with high ϵ' or conductive particles with high conductivity (i.e., argentum, Ag [23], nickel, Ni [24], zinc, Zn [25], cuprum, Cu [26]) are often dispersed into a polymer matrix for improved dielectric properties and good flexibility. However, the minimum 50 vol% loading of ceramic particles is needed for a decent increase in the ϵ' of the composites, which inevitably leads to deteriorated mechanical strength and flexibility, as well as the loss of good processability [27–31]. At the same time, it always results in unwanted high dielectric loss and low E_b in polymers due to the inhomogeneous dispersion or partial agglomeration of fillers in matrix. Alternatively, to cope with this dilemma, a small amount of conductive fillers are often introduced into polymers to prepare percolating composites with excellent physical properties.

Based on the percolation theory, when the fillers content nears the percolation threshold (f_c), the conductive particles will form micro-capacitors within the polymer and contributes significantly to interface polarizations (IP), thereby leading to a significant increase in the ϵ' of the composites. But, once the fillers content approaches or exceeds the f_c , the direct contact between the adjacent conductor fillers occurs, and results in the formation of electron pathways or network, thus inevitably bring about enormous dielectric loss and large leakage current. This possesses a tremendous threat to the long-term serviceability of dielectrics for electronic devices. Therefore, the precise control of the f_c of the conductive fillers in polymers is a critical issue, and fully realizing the balance between enough large ϵ' , high E_b as well as low loss is currently still a challenge in preparing polymer composites with overall high dielectric performances.

In recent years, core–shell structure, i.e., conductive core@insulating shell, has attracted much attention due to versatile advantages like favorable thermal or electrical stability, and the conductive core particle is subjected to the protection from the shell subsequently leading to multifarious properties resulted from the constituent components [32]. Through fine designing and preparation of core–shell structured particles, polymer composites with high ϵ' but low dielectric loss can be fully realized. When compared with high cost and complicated chemical route for the preparation of core–shell structured particles, direct oxidation method shows favorable advantages such as low cost and facile preparation. Nowadays, a lot of research work suggests that coating oxide shell on the surface of conductive fillers is a rather simple and efficient strategy for enhanced dielectric properties, e.g., Ni@NiO [33], Al@Al₂O₃ [34], Cu@CuO [35], Zn@ZnO [36], and others. The metal core increases the electron migration because of its high conductivity, while the insulating shell blocks the direct contact between the conducting fillers to inhibit electron migration; so, based on this interfacial barrier effect, the electron displacement within an individual metal particle still remains active and even enhanced by the presence of multiphase interfaces. Thus, fillers with a core–shell structure can easily achieve markedly suppressed dielectric loss and high E_b in composites at a high level of filler loading.

Compared to other metal fillers, as a kind of conductive filler, nickel (Ni) has special electrical and magnetic properties and is used in a wide range of applications such as conductor, magnet, electrical sensors and catalysts, et al. Some studies have shown that the Ni filled polymers showed ultrahigh dielectric permittivity as well as large loss near to the f_c owing to the presence of leakage currents [37]. To suppress the large loss, some insulating shells like NiO, silica, polystyrene, and others were often constructed on the surface of core Ni [24, 33], and the corresponding composites exhibited much inhibited dielectric loss but still holding high permittivity. For instance, Li T., et al. coated the surface of Ni particles with a layer of SiO₂ by a sol–gel process, and prepared the Ni@SiO₂/PVDF composites [24]; due to the presence of the insulating SiO₂ shell, the dielectric loss was inhibited to very low levels, e.g., with a filler content of 30 wt% the dielectric loss at 100 Hz for pure Ni/PVDF and Ni@SiO₂/PVDF are 2.24 and 0.05, separately [29]. Additionally, the formation of a layer of insulating NiO external shell on the surface of the raw Ni powders also prominently reduced the loss and concurrently enhanced both ϵ' and thermal conductivity of the Ni@NiO/PVDF composites thanks to the presence of the NiO interlayer improving interfacial interactions and polarizations, and suppressing the loss [33].

Alumina, i.e., Al₂O₃, holds excellent electrical insulation performance because of its high E_b (8–43 kV/mm) and very large band gap (8.9 eV) [38], and is wider used for microelectronic devices and power equipment. As an insulating shell, it can significantly suppress leakage currents and inhibit high field dielectric loss in polymer composites. For example, Zhou et al. prepared Al@double-Al₂O₃ core–shell structured particles by adjusting the calcination time under a nitrogen atmosphere and the Al₂O₃ interlayer not only enhanced the permittivity thanks to multiple IP, but also largely reduced the loss and conductivity of the composites [34]. Hitherto, the dielectric properties of Ni@Al₂O₃/PVDF have been rarely investigated as a function of fillers content and the Al₂O₃ thickness. So, in this work, a facile sol–gel method was adopted to construct core–shell Ni@Al₂O₃ particles, and the dielectric properties of Ni@Al₂O₃/PVDF composites were investigated in relation to the filler loading, frequency and Al₂O₃ shell thickness. The results will shed a light on understanding the correlation

between microstructure and dielectric performances of the composites with high ϵ' but low loss, and enhanced E_b .

2 Experimental

2.1 Materials

Spherical Ni powders with an average particle size of about 1–3 μm were obtained from Hebei Tuyu Metal Material Co., China. PVDF FR903 was purchased from 3F New Materials Co. (Shanghai, China) as polymer matrix. *N, N*-dimethylformamide (DMF) was obtained from Tianjin Chemical Reagent Co., China. Glycol ether, isopropanol aluminum, and acetyl acetone were reagent grade, and purchased from Shanghai Baishun Biotechnology Co., China. Acetic acid was from Tianjin Fuyu Fine Chemical Co., China.

2.2 Preparations of samples

The preparation process of the Ni@Al₂O₃ particles and the Ni@Al₂O₃/PVDF composites is depicted in Fig. 1. As indicated, the core–shell structured Ni@Al₂O₃ particles were prepared by a sol–gel process. First, a certain amount of Ni and aluminum isopropanol (5 wt%, 10 wt%, 15 wt%, 20 wt% of Ni particles, respectively) were dispersed in 50 mL of glycol ether and agitated for 30 min with the magnetic stirring at 60 °C. Next, 2 mL of acetylacetone was added and stirred for additional 30 min. After that, 10 mL acetic acid was added into this mixture and magnetically stirred at 90 °C for 36 h. Then, the mixture was centrifuged several times, and the sediment was dried in an oven at 60 °C for 12 h. At length, the obtained sample was heated in a tube furnace at 800 °C for 2 h under N₂ atmosphere to gain the surface-modified Ni, i.e., Ni@Al₂O₃. For convenience, the resultant samples are denoted as Ni-1 (Ni@5 wt% Al₂O₃), Ni-2 (Ni@10 wt% Al₂O₃), Ni-3 (Ni@15 wt% Al₂O₃) and Ni-4 (Ni@20 wt% Al₂O₃), separately, corresponding to the pure Ni particles represented as Ni-0.

The Ni@Al₂O₃/PVDF composites were prepared by solution blending followed by hot-pressing. Firstly, 5 g of PVDF was dissolved into DMF to form PVDF solution at 50 °C, and desirable number of Ni@Al₂O₃ particles were put into the DMF solvents

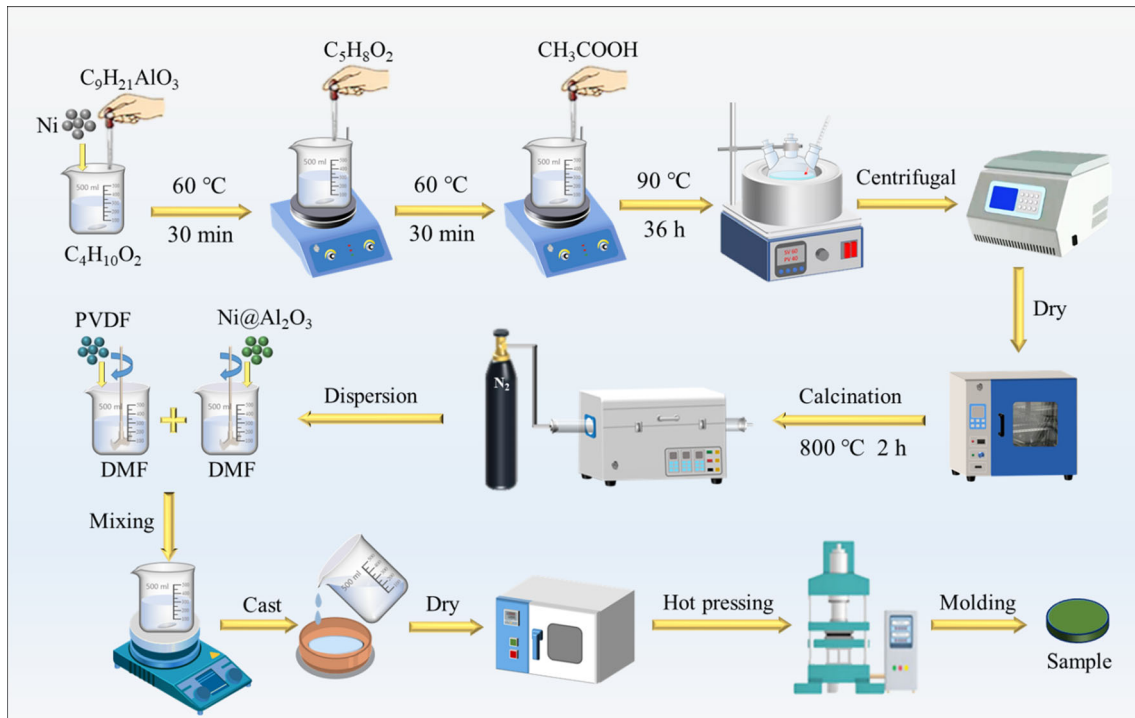


Fig. 1 Synthesis of Ni@Al₂O₃ particles and preparation of the corresponding PVDF composites

under for 30 min by sonication. Then, the Ni@Al₂O₃/DMF suspension was added to the PVDF solution, and the resulting mixture was further stirred for 8 h at room temperature. After that, the mixture was poured onto a clean glass plate and dried in a vacuum oven at 120 °C to absolutely evaporate the surplus DMF solvent. In the end, the dry films were stacked up and compression molded at 220 °C at a pressure of 12–15 MPa for 15 min.

2.3 Characterizations

The surface chemistry of the samples was measured using a Fourier-transform infrared (FT-IR) spectrometer (Perkin-Elmer, Paragon1000) in the spectrum range of 4000–400 cm⁻¹. The weight change of sample after heating was measured with a thermal weight gravimetric analyzer (TGA, SDTA851, Swiss) at a heating rate of 10 °C/min from 50 to 800 °C under air atmosphere. The structure analysis of the pristine Ni and Ni@Al₂O₃ particles, and composites were performed by a Shimadzu X-ray diffractometer-6000 (XRD) equipped with a graphite monochromatic instrument and a Cu cathode (40 kV, 30 mA, scanning rate 2°/min). The surface elemental analysis of Ni@Al₂O₃ particles was carried out using X-ray

photoelectron spectroscopy (XPS, Thermo Scientific K-Alpha, Japan). A JEOL JSM-7000F scanning electron microscope (SEM) was used to observe the fracture morphology of the specimens. The fracture surfaces were prepared in N₂ liquid and observed after sputtering with a layer of gold in a vacuum. The core-shell structure images of the pure Ni and Ni@Al₂O₃ were observed using an H-800 transmission electron microscope (TEM) purchased from Hitachi, Japan.

Dielectric measurements of the samples were recorded with a Novocontrol Technologies Alpha-N high-resolution dielectric analyzer from Germany. The shape of the specimens was a circular disc (diameter = 20 mm and thickness ~ 1 mm). Before measurement, a layer of Cu foil is applied to both the upper and lower surfaces of the specimen as electrodes. The samples for E_b properties are placed directly between two opposing copper-ball electrodes and are loaded with a continuous alternating current (AC) voltage by a 50 kV, 50 Hz transformer. Both electrodes and samples are immersed in an insulating oil to prevent surface discharges and flashover. The lower electrode is earthed and the upper electrode is subjected to increasing AC voltage at a rate of 2 kV/s

until the specimen fails. At the end of the test, the ultimate breakdown voltage is recorded.

3 Results and discussion

3.1 Microstructures of core–shell Ni@Al₂O₃ and PVDF composites

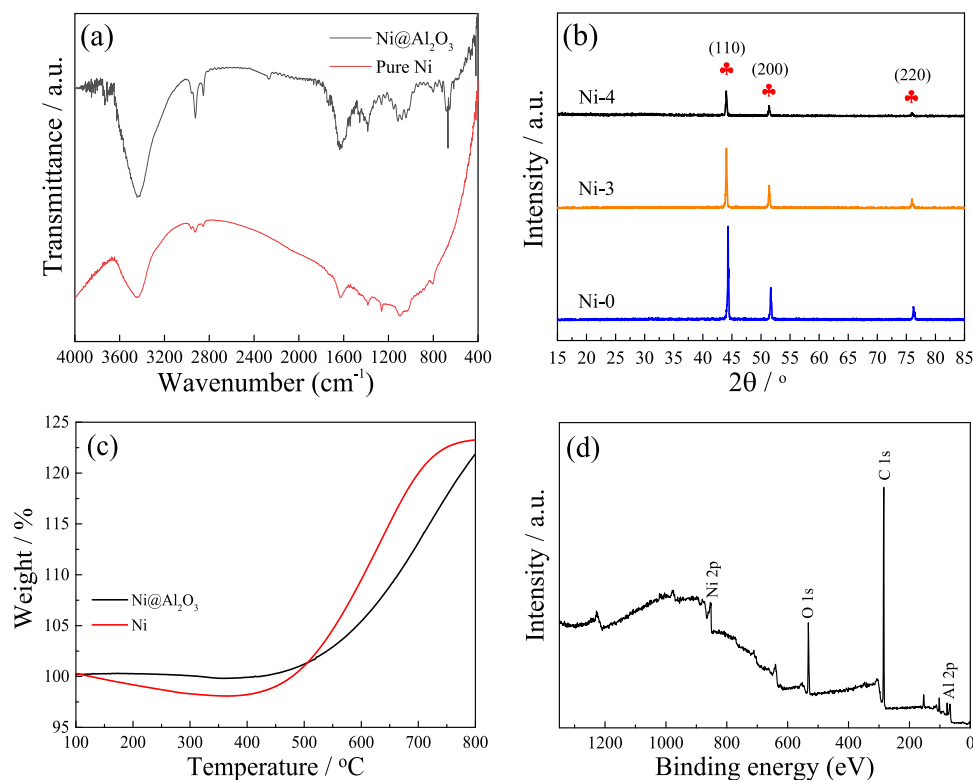
FT-IR spectroscopy provides useful information about the chemical structure of samples. Figure 2a shows the FT-IR spectra of pristine Ni and Ni@Al₂O₃ particles, respectively. Two obvious wide absorption peaks at 3400–3600 cm⁻¹ and 1610 cm⁻¹ are surveyed, separately, which are characteristic of the stretching vibration of hydroxyl (–OH) group peaks from the H₂O absorbed in the filler particles. Compared with pure Ni, the Ni@Al₂O₃ particles show obviously intense –OH groups resulting from the Al₂O₃ external shell on the surface of Ni. The absorption peak intensity of pure Ni particles at about 670 cm⁻¹ is reduced and the Ni@Al₂O₃ filler exhibits a new absorption band at about 419 cm⁻¹, corresponding to the stretching vibration of Al–O bonds in the Al₂O₃. Therefore, the above results

demonstrate the successful coating of a layer of Al₂O₃ on the surface of Ni particles.

Figure 2b shows the XRD patterns of Ni-0, Ni-3, and Ni-4 particles. All XRD patterns display three obvious characteristic peaks at 44.8°, 51°, and 76°, corresponding to the (110), (200), (220) diffraction planes for the pure Ni, individually. Compared with the XRD pattern of Ni-0, no new diffraction peaks can be observed for the Ni-3 and Ni-4. Differently, it is observed that the intensities of the three characteristic peaks decrease, suggesting that the Al₂O₃ is amorphous, and has an impeding effect on the XRD peaks of Ni particles.

Thermal stability of the Ni and Ni@Al₂O₃ particles were investigated using TGA, and the results are described in Fig. 2c. First, for pure Ni, a slow decrease in weight from 100 to 300 °C is observed because of the evaporation of adsorbed water or other small molecules absorbed in the samples. After that, the weight starts to increase remarkably from 400 °C and is stabilized from 750 °C, which is considered to be the formation of its oxides like NiO, thereby protecting it from further oxidation thanks to its passivated effect. In contrast, for the Ni@Al₂O₃ samples, the obvious weight gain is postponed at 450 °C, and it is much lower than that of pure Ni. The

Fig. 2 a FT-IR, b XRD and c TGA for pure Ni and Ni@Al₂O₃, and d XPS of Ni@Al₂O₃



reason is attributed to the fact that the amorphous Al_2O_3 shell outside of Ni powders has good oxidation-proof capability, thereby suppressing the further high temperature oxidation of Ni. Hence, TGA curves prove the existence of a layer of Al_2O_3 on the surface of pristine Ni particles.

To further analyze the elemental composition, XPS is performed on the $\text{Ni@Al}_2\text{O}_3$ particles. From Fig. 2d, it can be seen that the O 1s peak and Al 2p peaks corresponding to Al_2O_3 appear, indicating the presence of Al_2O_3 . Therefore, the above analyses comprehensively prove the successful preparation of $\text{Ni@Al}_2\text{O}_3$ core-shell structured particle.

Figure 3 shows the morphologies and microstructures pictures of Ni, $\text{Ni@Al}_2\text{O}_3$ and their PVDF based composites. From Fig. 3a, b, it can be seen that the diameter size of the raw Ni powders with smooth surface is approximately 1–3 μm , whereas, the $\text{Ni@Al}_2\text{O}_3$ particles emerges slightly rugged surface owing to the encapsulation of the Al_2O_3 shell. From the TEM image in Fig. 3c, no noticeable external shell

can be found for the pristine Ni, whereas, it can easily be noticed a layer of Al_2O_3 shell on the surface of $\text{Ni@Al}_2\text{O}_3$ powders in Fig. 3d, i.e., the formation of core-shell structured $\text{Ni@Al}_2\text{O}_3$ particles. The TEM measurements provide direct evidence for the core-shell structured $\text{Ni@Al}_2\text{O}_3$ particles obtained in this experiment. Figure 3e–i displays the SEM images of pristine Ni/PVDF and $\text{Ni@Al}_2\text{O}_3$ /PVDF composites with diverse filler loadings. It can be clearly noted that the raw Ni particles were heterogeneously dispersed in the PVDF with clear agglomeration of fillers. While, the $\text{Ni@Al}_2\text{O}_3$ fillers were relatively uniformly dispersed in the matrix without distinct aggregation compared with the raw Ni. The improved dispersion of filler can be attributed to the enhanced phase interfacial interactions between $\text{Ni@Al}_2\text{O}_3$ and PVDF via the hydrogen bond interactions between the $-\text{OH}$ in Al_2O_3 and F atom in PVDF. Therefore, the presence of the Al_2O_3 interlayer improves the interfacial compatibility between the filler and the matrix, and promotes the even

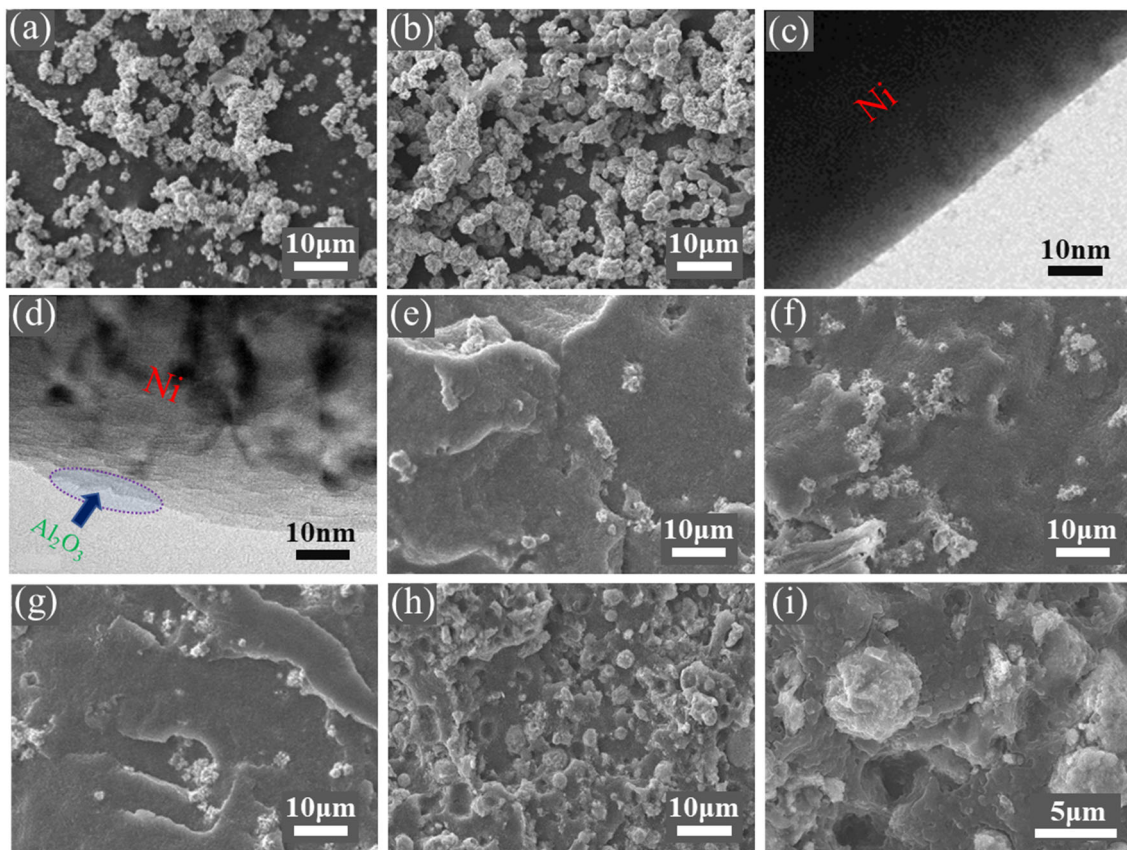


Fig. 3 TEM images of Ni (c) and $\text{Ni@Al}_2\text{O}_3$ (d), and SEM images of Ni (a), $\text{Ni@Al}_2\text{O}_3$ (b), 30 wt% Ni/PVDF (e) and 50 wt% Ni/PVDF (f), 30 wt% $\text{Ni@Al}_2\text{O}_3$ /PVDF (g) and 50 wt% $\text{Ni@Al}_2\text{O}_3$ /PVDF (h, i)

dispersion of Ni particles in the matrix, which can be easily observed in the high magnification SEM, as indicated in Fig. 3i.

3.2 Dielectric properties

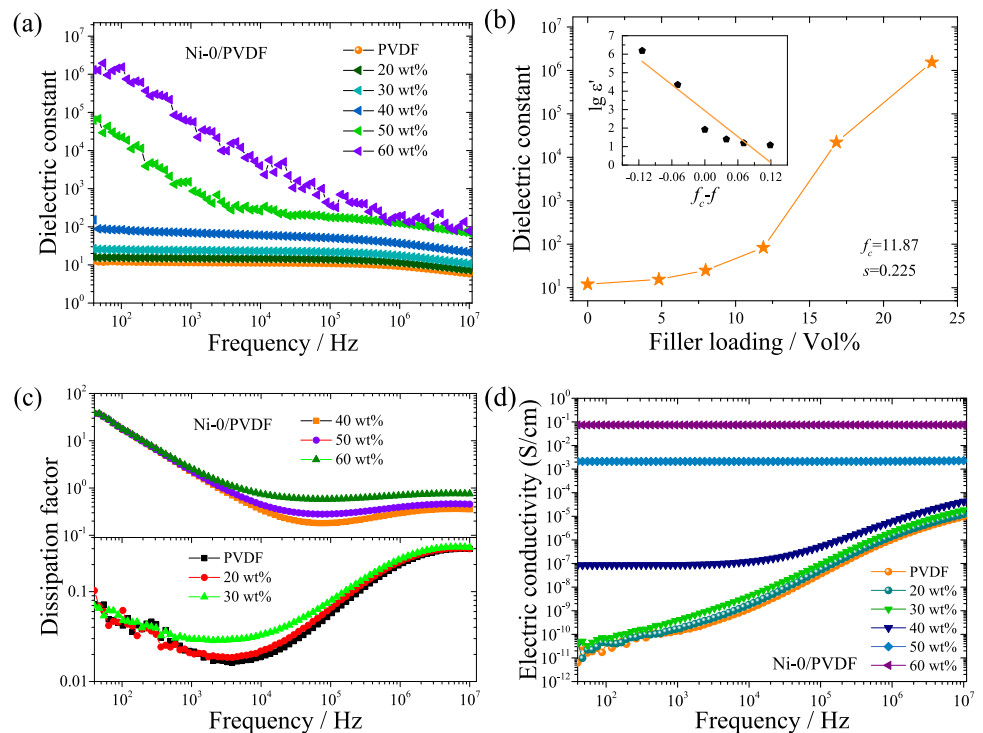
Figure 4 exhibits the influences of filler loading and frequency on the ϵ' , dielectric loss, and conductivity of the Ni-0/PVDF composites. To begin with, we first discuss the ϵ' of the composites. Usually, the ϵ' of composites indicates the ability of store charges in the presence of an electric field. From Fig. 4a, the ϵ' of the Ni-0/PVDF composite goes up with increasing the conductive filler content, typical for the percolating systems. This phenomenon can be ascribed to the IP, as also called the Maxwell–Wagner–Sillars (MWS) effect, and it occurs on non-homogeneous phases with different conductivities and ϵ' [39, 40]. For Ni-0/PVDF composites, a huge number of charge carriers are trapped and barred at the interfaces between the PVDF matrix and the Ni filler owing to the huge difference in electric conductivities between them when an external electrical field is applied, thereby causing to strong IP effect and leading to large permittivity of the composite. In addition, the ϵ' decreases with increasing frequency, in particular, more significantly at high frequencies. This

phenomenon is attributed to the suspension of the contributions from orientation, ionic polarizations aroused in the speed changes in high frequency [41]. The ϵ' of all composites displays a weak frequency dependence when the filler content is less than 30 wt%. At a low filler content, The Ni powders are set at a relatively large distance from each other, so leading to low IP. However, when the Ni filler content is approaching the f_c like 40 wt%, the ϵ' increases sharply, suggesting the emergence of percolation phenomena. For example, the ϵ' at 100 Hz are 84 (40 wt%), 22,221 (50 wt%), and 1,538,870 (60 wt%), respectively. The reason can be attributed to the formation of a conductive network within the PVDF. When the electrons are competent of hopping/tunneling through many adjacent conductive filler particles, the charges which were bound in the isolated conducting particles are activated and released, thus causing a dramatic enhancement in ϵ' . The dielectric properties of the percolative composite will undergo a sudden change at the f_c , which is determined by the Eq. (1).

$$\epsilon = \epsilon_m (f_c - f)^{-s} \quad \text{for } f < f_c, \tag{1}$$

where ϵ_m represents the ϵ' of the polymer matrix, and s denotes a critical exponent of about 1. The best linear fitting exhibits an f_c value of Ni-0/PVDF

Fig. 4 Frequency dependence of **a** dielectric constant, **c** dissipation factor, **d** electric conductivity of Ni-0/PVDF composites with different filler loading, and **b** dielectric constant as a function of filler loading at 100 Hz for Ni-0/PVDF, the inset shows a log–log plot of dielectric constant as a function of $f_c - f$



composites of 11.8 vol% (about 30 wt%), which is consistent with the experimental results.

Generally, the dielectric loss can be supposed to the sum of electrical leakage loss and polarization loss in the studied frequency boundary. The frequency dependence of the loss of raw Ni-0/PVDF composites with different filler contents is shown in Fig. 4c. As can be obviously observed from Fig. 4c, the dielectric losses of composites with various filler contents show the same trend, i.e., they first decrease with increasing frequency until a moderate frequency, and furthermore increase as the frequency increases. The dielectric response at low frequencies is a typical IP behavior, mainly from charge carriers trapped at non-uniform interfaces between diverse phases. However, the dielectric response at high frequencies is mainly generated by the directional polarization of the C–F dipole of PVDF, also known as Debye relaxation behavior [42]. The variability in loss of the Ni-0/PVDF composites is nearly independent of Ni filler when the filler loading is lower than f_c ; whereas, when the filler loading attains or exceeds the f_c , the loss of Ni-0/PVDF suffers an acute rise at low frequencies because of the formation of direct current (DC) conduction resulted from the percolated filler network. The imaginary part of ϵ' (ϵ'') in composites can be formulated by the following Eq. (2).

$$\epsilon'' = \epsilon''_{dc} + \epsilon''_{MW} + \epsilon''_D \quad (2)$$

where ϵ''_{dc} and ϵ''_{MW} is on behalf of conduction and IP, separately, and ϵ''_D denotes the dipole loss.

The conduction loss is determined by the following Eq. (3):

$$\epsilon''_{dc} = \frac{\sigma_{dc}}{2\pi \cdot f} \quad (3)$$

where σ_{dc} and f are related to the DC conductivity and frequency, separately.

From Eqs. (2) and (3) above, it is clear that the contribution from leakage conduction loss is greater for the pristine Ni/PVDF composites with high filler content at low frequency ranges.

Figure 4d plots the frequency dependence of the AC conductivity for Ni-0/PVDF composites with different filler loadings. When the Ni-0 content is under the f_c , the conductivities of the Ni-0/PVDF composites slightly increase as the filler loading increases, which could be attributed to the occurrence of a small quantity of electron tunneling. When the

filler content further increases to f_c and even greater, the Ni powders are in contact with each other and therefore form conductive networks in the composites, resulting in a significant increase in leakage current. So, the AC conductivity values experience a dramatic increase at low frequencies, and appear a DC conduction independent of frequency [43].

Figure 5 plots the frequency dependence of the dielectric properties on the filler content for Ni@Al₂O₃/PVDF composites. From which, we can see that the ϵ' , loss and conductivity of Ni@Al₂O₃/PVDF composites have a similar trend as the pristine Ni/PVDF, respectively, and the dielectric properties of all the composites change nearly linearly with increasing filler content. In comparison to Ni-0/PVDF composites, the Ni@Al₂O₃ fillers prepared by four distinct conditions obviously reduce the ϵ' of all composites, but they are still much high than that of pure PVDF because the amorphous shell inhibits the charge accumulation at the interface between fillers and PVDF. No percolation phenomenon occurs even at an f greater than f_c . Thus, the suppressed ϵ' is mainly associated with the formation of the insulating Al₂O₃ shell as an interlayer between the Ni particles and the PVDF matrix, which not only validly impedes charge migration between fillers and restrains charge displacement, but also reduces space charge polarizations.

The loss curves of Ni@Al₂O₃/PVDF are depicted in Fig. 5b. Usually, the conduction loss is the primary factor for the great dielectric loss at low frequencies. Unlike the raw Ni/PVDF, the loss values of Ni@Al₂O₃/PVDF composites with high filler levels are remarkably reduced to rather low levels and exhibit less frequency dependence at low frequencies. Further, as indicated in Fig. 5c, no DC conduction process is found for Ni@Al₂O₃/PVDF because the insulating Al₂O₃ interlayer effectively protects the Ni particles from direct contact with each other, and significantly suppresses the loss through reducing the leakage current. Using Eq. (3) we can infer to that the contribution from conduction loss in Ni@Al₂O₃/PVDF becomes minimal. The AC conductivity of the four Ni@Al₂O₃/PVDF composites has a nearly linear relationship between filler loading and frequency dependence, suggesting the typical insulation properties of the composites studied. Therefore, the insulating Al₂O₃ shell exerts a positive influence on the suppression on loss and AC conductivity of Ni@Al₂O₃/PVDF composites, thereby reducing the

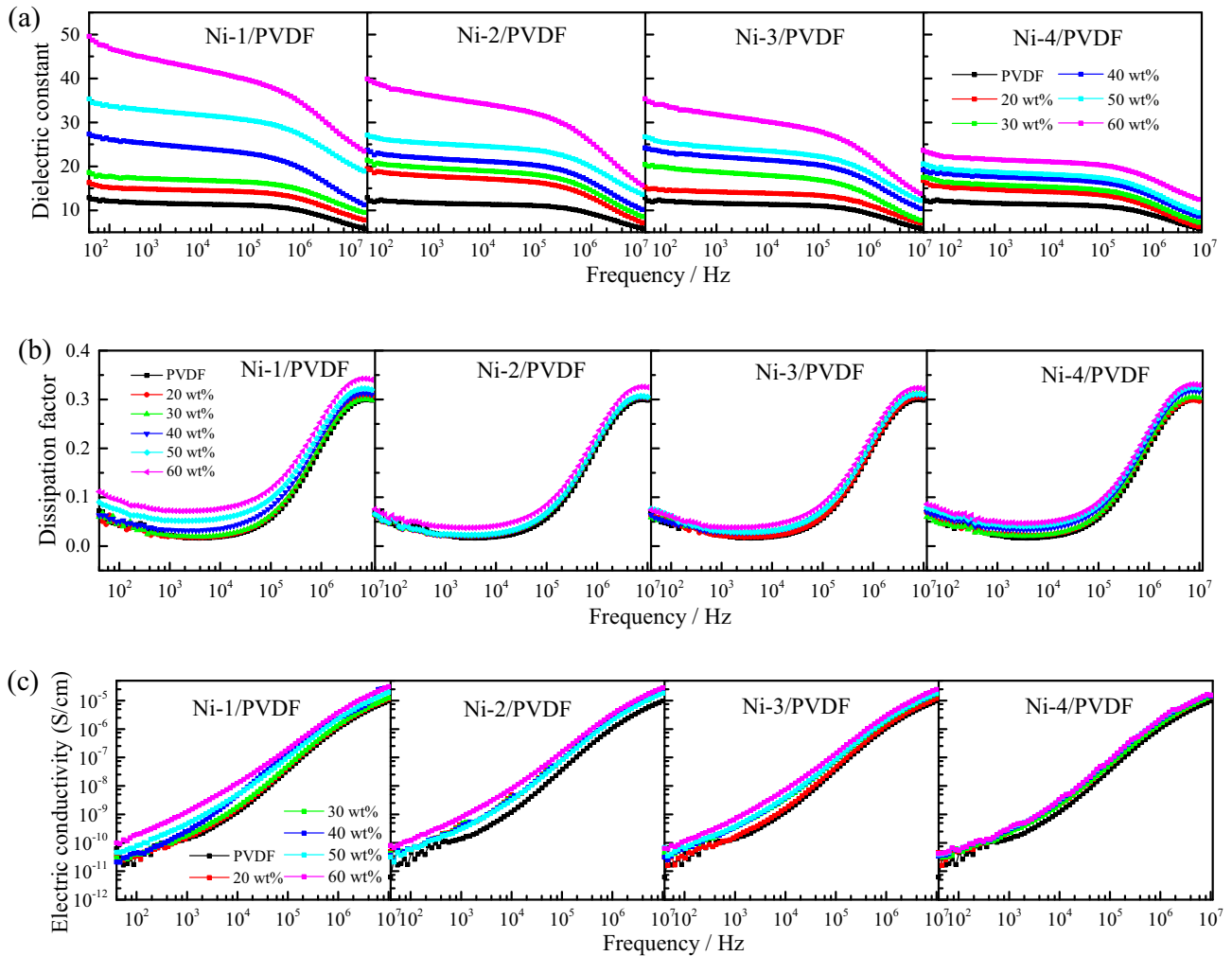


Fig. 5 Frequency dependence of **a** dielectric constant, **b** dissipation factor, and **c** electric conductivity of Ni@Al₂O₃/PVDF composites with different filler loadings

sensitivity to high electric field and guaranteeing the safe operation of the dielectrics.

Figure 6 depicts the impact of the insulating Al₂O₃ shell’s thickness on dielectric properties of Ni@Al₂O₃/PVDF. Comparing the dielectric properties among Ni-1/PVDF, Ni-2/PVDF, Ni-3/PVDF, and Ni-4/PVDF, it is obviously found that the ϵ' , the ϵ'' , and the conductivity of the Ni@Al₂O₃/PVDF composites decrease with increasing the shell thickness of Al₂O₃. The reducing trend is due to the fact that as the Al₂O₃ shell’s thickness becomes thicker, the interlayer inhibition effect on the charge carrier’s migration is much pronounced. Therefore, the insulating Al₂O₃ shell effectively blocks electron transfer between adjacent conductive particles, thereby making the electron displacements more confined within the individual filler, and resulting in prominently

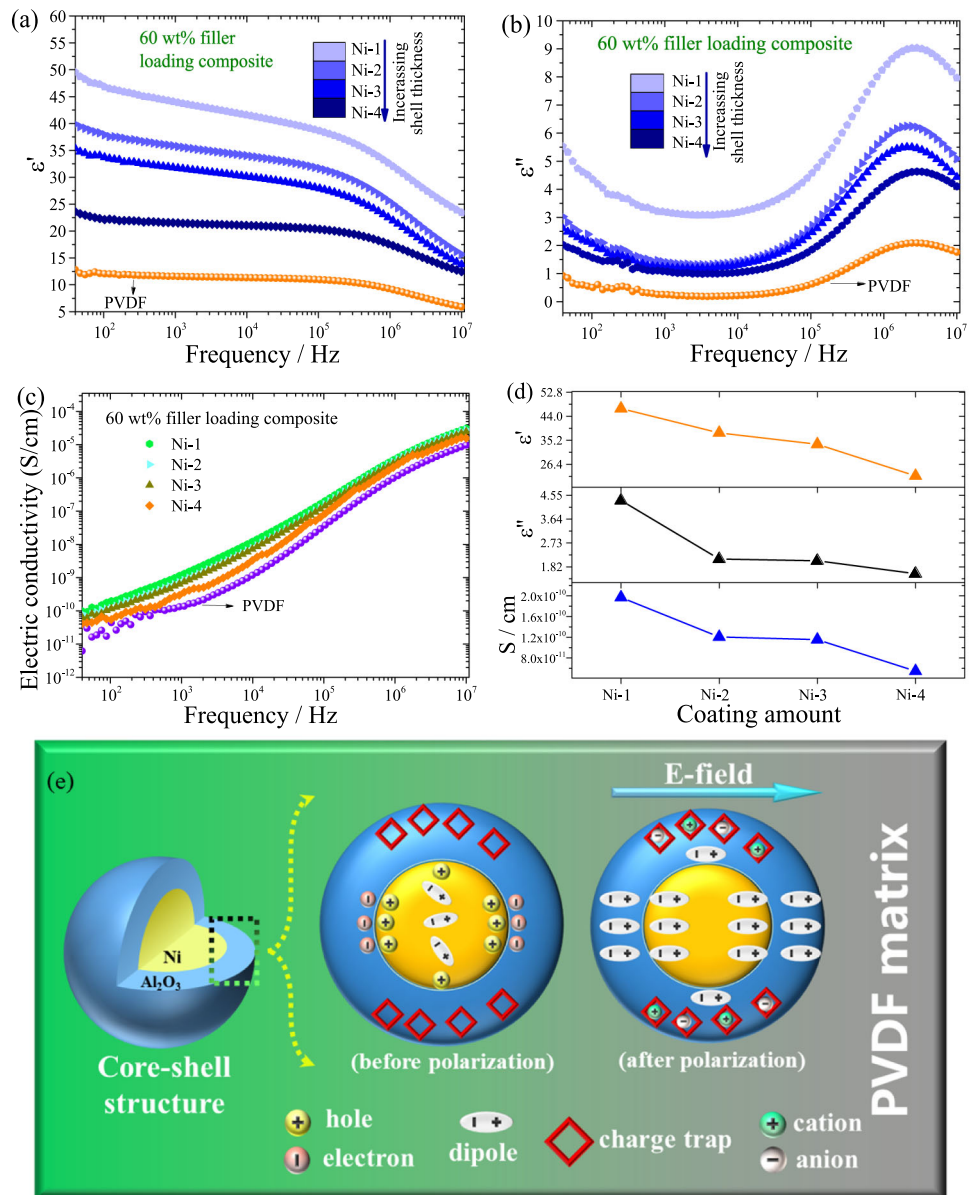
suppressed loss and conductivity of the composites, as indicated in Fig. 6e. Therefore, this interlayer not only weakens the IP effect but also effectively inhibits the electron tunneling and long-range migration, and the resulting low loss polymer composites still have much high ϵ' compared with pure PVDF [44].

To further discuss the mechanism of the effect of different fillers on the dielectric properties of the composites, separate polarization contributions need to be isolated from the dielectric spectra of the composites. This can be obtained by fitting the experimental data with Havriliak-Negami (HN) expressions:

$$\epsilon^*(w) = \epsilon_\infty + \sum_{j=1}^2 \frac{\Delta\epsilon_j}{1 + (i w \tau_j)^{\alpha_j}} + \frac{\sigma_{dc}}{i w \epsilon_0}, \quad (4)$$

where w denotes the angular frequency, α_j represents the shape parameter indicating the relaxation time

Fig. 6 The ϵ' , ϵ'' and conductivity of the composites with a fixed 60 wt% content of filler for different systems (a–d), and schematic diagram for the effect of interface on the carriers migration in Ni@Al₂O₃/PVDF (e)



distribution of j mode, $\Delta\epsilon_j$ and τ_j are the dielectric relaxation strength and characteristic relaxation time of j mode, separately, and σ_{dc} and ϵ_0 indicate the free space conductivity contribution and ϵ' , respectively.

Figure 7a–d displays the deconvolution of the dielectric spectra for different PVDF composites, and plots the contribution of every relaxation mode. There are two forms of relaxation in the dielectric response of the composites. One is the amorphous PVDF (α relaxation), which occurs in the frequency of 10–30 MHz. Another contribution comes from the polarization of the core–shell fillers. Under the application of an applied electric field, the electrons in the metal Ni core will be separated and positioned

within the insulating Al₂O₃ shell, forming an asymmetric charge distribution that acts as an electric dipole [34, 42]. In addition to the above two relaxations, the dielectric loss of the composites (i.e., quasi-DC conductivity loss) increases dramatically in the low frequency ranges due to the long-range migration of the residual charges, like impurities, chemical leftovers, ions, etc. Usually, the electron displacement includes both electron transfer between the core–shell interface (fast interfacial polarization) and charge migration between particles (slow interfacial polarization), and both of them are essentially related to IP. Obviously, the dielectric properties of

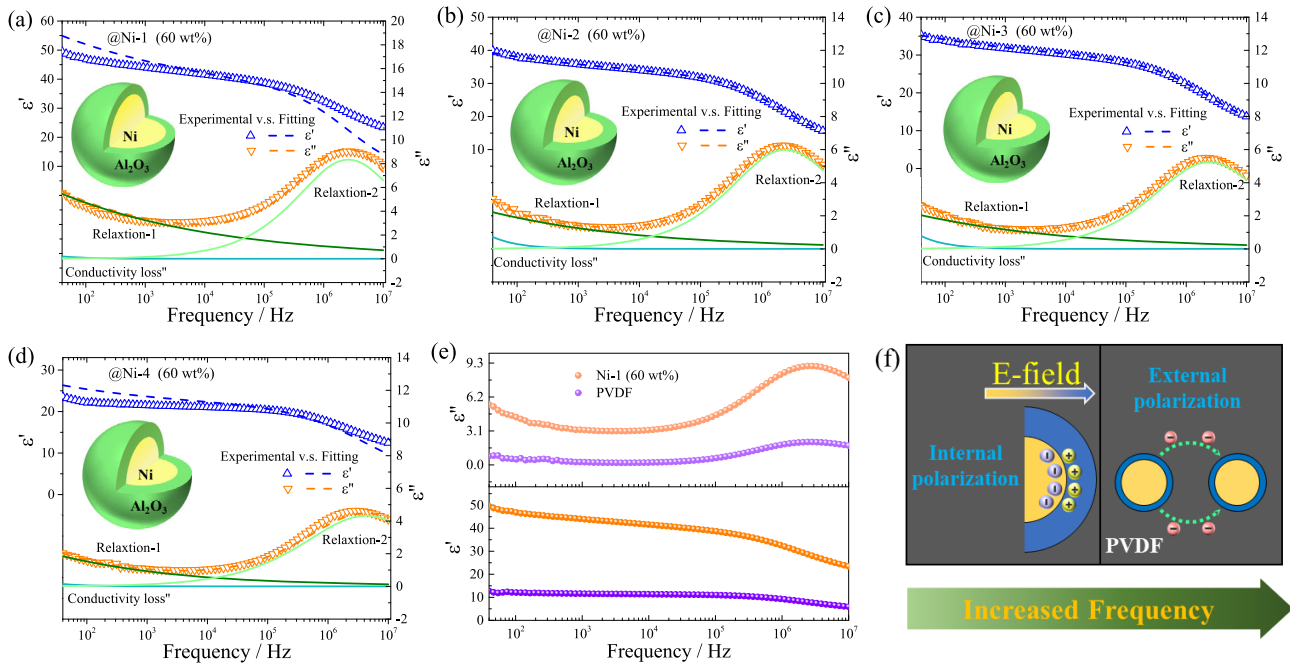


Fig. 7 Deconvolution of dielectric spectrum of PVDF composites containing 60 wt% filler, both the ϵ' and ϵ'' are fitted by the HN equation (a–d), comparison of ϵ' and ϵ'' for 60 wt% Ni-1/PVDF

the composites depend on these two types of IP [34]. Figure 7e compares the ϵ' and ϵ'' for Ni-1/PVDF composite and pure PVDF. At low frequencies, it is clear that the ϵ' of Ni-1/PVDF composite is significantly higher than pure PVDF, which is attributed to the predominance of fast IP. Figure 7f shows a schematic diagram of polarization between particles and polarization within particles. At low frequencies, under the presence of an applied electric field, charge carriers at the particle interface of the core–shell structure form electric dipoles to enhance IP. At high frequencies, the intraparticle response diminishes, when electron transfer between particles plays a major role.

Figure 8 presents the E_b and the characteristic Weibull distribution curve of Ni/PVDF and Ni@Al₂O₃/PVDF composites. From Fig. 8a, the E_b increases with an increase in the thickness of Al₂O₃ shell under the same filler concentration. For example, when the filler loading is 20 wt%, the characteristic E_b of the Ni@Al₂O₃/PVDF composite are 8 kV/mm (Ni-1), 11 kV/mm (Ni-2), 14 kV/mm (Ni-3), and 20 kV/mm (Ni-4), respectively. The E_b of the composites is markedly enhanced in comparison with pure Ni-0/PVDF. The insulating Al₂O₃ shell acts as an effective buffer interlayer that not only reduces the

composites and PVDF (e), and schematic diagram for polarizations between and within particles (f)

discrepancy in conductivity and permittivity between Ni and PVDF, but also significantly alleviates the local electric field distortion and mitigates the corresponding local electric field concentration effect. Therefore, the presence of alumina shell leads to an enhanced E_b in composites when compared with raw Ni. Further, the insulating interlayer introduces deep traps for electron migration which effectively inhibits and frustrates the charge carrier’s long-range migration in the matrix. And with further increasing the thickness of Al₂O₃ shell obviously results in a noteworthy increase in E_b of the composites, subsequently blocking the formation of leakage current across the composites under high electric field. In addition, the E_b apparently decreases with increasing filler contents for five composites, as shown in Fig. 8a. For instance, the E_b decreases rapidly from 20 kV/mm (20 wt%) to 5.5 kV/mm (60 wt%) for Ni-4/PVDF. Further increasing the content of Ni@Al₂O₃ particles will result in increased charge carrier’s accumulation and structural defects at the phase interfaces, thus leading to a decreased E_b [45].

The E_b is discussed utilize a two-parameter Weibull distribution function as expressed in the Eq. (5), and the results are displayed in Fig. 8b–e:

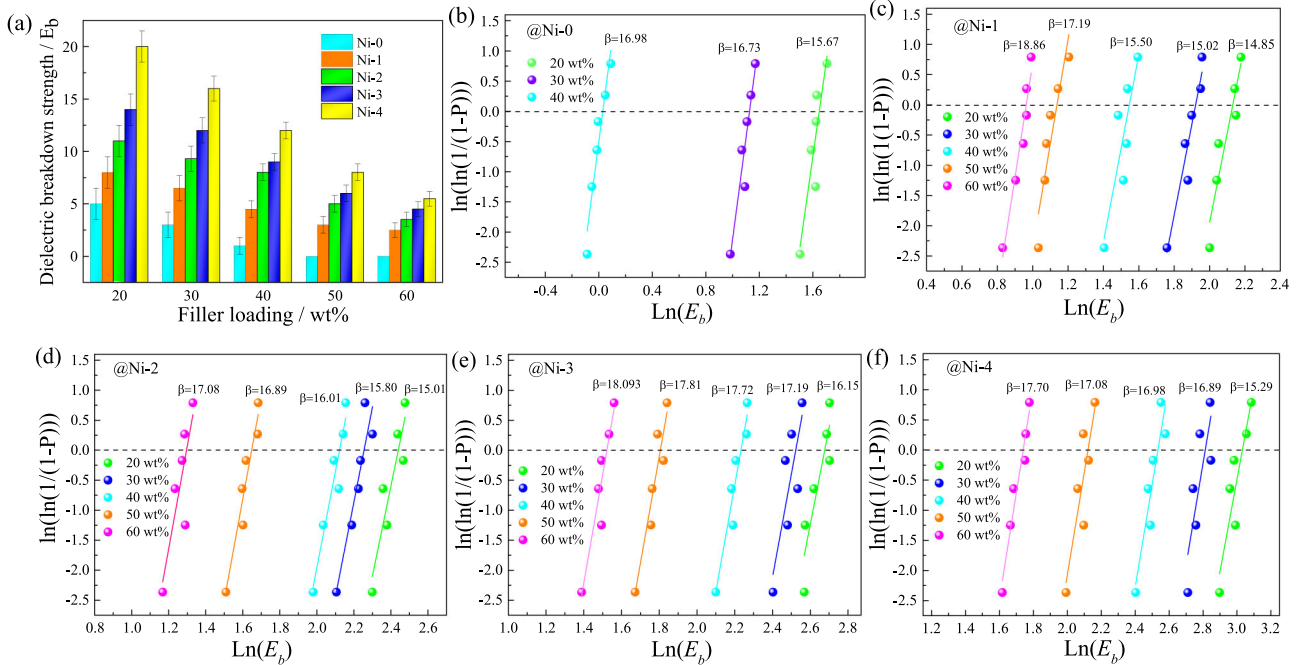


Fig. 8 **a** E_b variations with filler content for five composites and **b–f** E_b Weibull distribution of five systems

$$P = 1 - \exp \left[- \left(\frac{E}{E_0} \right)^\beta \right], \tag{5}$$

where P denotes the cumulative probability of electrical failure, E stands for breakdown strength, E_0 represents the characteristic breakdown strength (cumulative probability of failure 0.632) and β is on behalf of the shape parameter.

The linear fit and Weibull parameters are illustrated in Fig. 8b–e, the linearity of all lines is fit for the distribution dot of the Weibull model, and the parameters are significantly greater than 1, indicating that the probability distribution of these E_b data coincides with a two-parameter Weibull analysis.

3.3 Cole–Cole curves

Dielectric material displays a complex IP under the action of alternating electric field, also known as dielectric relaxation phenomenon, and the Cole–Cole curves defined by the dielectric modulus (M) is an effective method to analyze the relaxation process. The M is defined as the inverse quantity of complex permittivity:

$$M^* = \frac{1}{\epsilon^*} = \frac{\epsilon'}{\epsilon'^2 + \epsilon''^2} + \frac{\epsilon''}{\epsilon'^2 + \epsilon''^2} = M' + M'', \tag{6}$$

where M' and M'' are real and imaginary part of the complex electric modulus.

Figure 9 presents the Cole–Cole curves of M' versus M'' for the PVDF filled with raw Ni and four types of Ni@Al₂O₃ particles with different filler contents [Eq. (6)]. As seen from Fig. 9, the Cole–Cole curves of all samples have two semicircular arcs. The first small radius arc occurs at high frequencies, which is linked to the dipole polarization in the Debye model. The second big radius arc appearing at low frequencies is associated with IP and DC leakage current. For Ni-0/PVDF composite as indicated in Fig. 9a, it can be seen that when the filler content exceeds 30 wt%, the semicircular arc undergoes a sudden change, which is caused by a sharp increase in DC conductivity. While, for Ni@Al₂O₃/PVDF composites in Fig. 9b–e, no DC behavior can be noticed, and remarkably compressed semicircular arcs are found, suggesting significantly suppressed loss and conductivity of the composites at low frequencies. In addition, by comparing the composites with fillers of 30 wt% and 60 wt%, respectively, as shown in Fig. 9f, it is obvious that with an increase of filler content, the relaxation peak of M'' gradually shifts towards low M' and decreases. The peak variation in the position in X axis where the small semicircle arc is placed reflects the change in DC

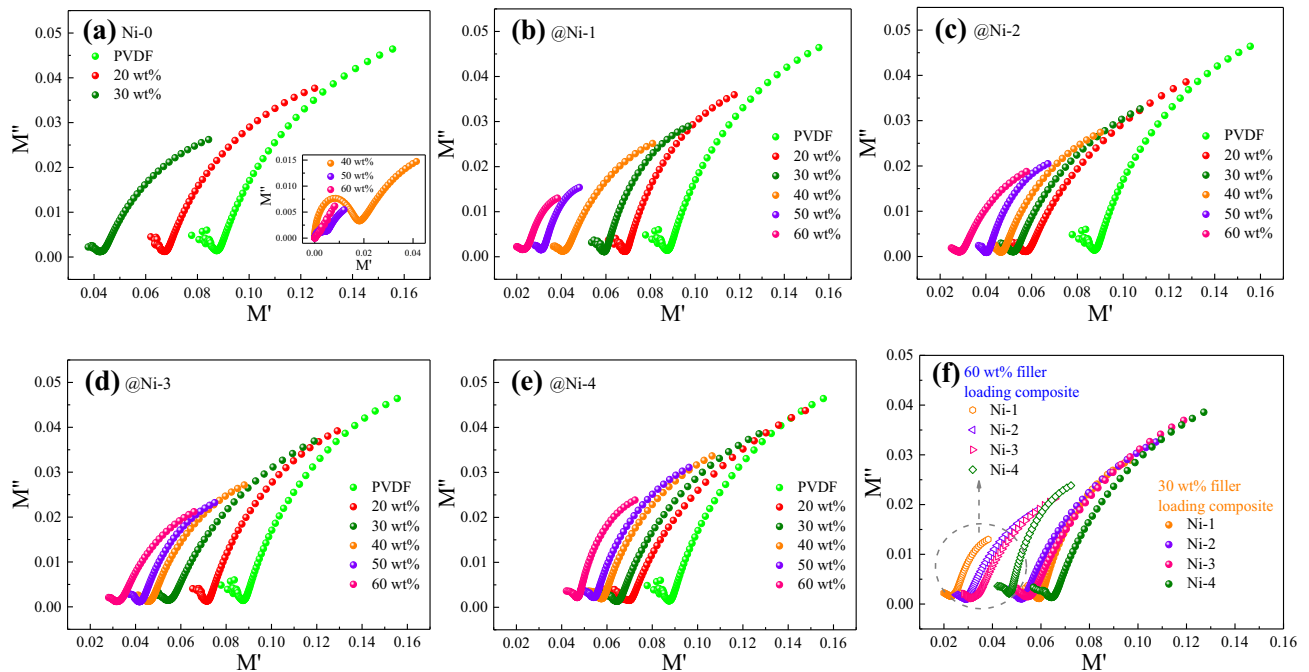


Fig. 9 Cole–Cole plots of M'' vs. M' for PVDF filled with pure Ni (a) and Ni@Al₂O₃ (b–e) with various filler loadings, and f M'' vs. M' for PVDF with 30 wt% and 60 wt% fillers

conductivity and loss of composites. It is found that increasing the filler content, the small arc slightly moves to left direction, indicating the increased loss and conductivity of composites.

4 Conclusion

To effectively inhibit the huge dielectric loss of raw Ni/PVDF, core–shell structure Ni@Al₂O₃ particles were fabricated through a facile sol–gel process and their PVDF composites were obtained through solvent-blending followed with hot-pressing. The FT-IR, XRD, TGA, XPS, and TEM measurements prove that an insulating Al₂O₃ layer was formed outside of the pristine Ni core. For the Ni@Al₂O₃/PVDF composites, the ϵ' reduces under the equal filler content thanks to suppressed IP effect, and the dielectric loss is significantly inhibited to very low levels. That is principally attributed to the formation of an insulating Al₂O₃ shell which effectively arrests the conductive Ni powders from direct contacts with each other, therefor blocking the long-range electron migration and resulting in low AC conductivity. Besides, with increasing the thickness of Al₂O₃ shell, the loss and AC conductivity remarkably decrease because of its gradually enhanced high electrical resistivity.

Significantly improved E_b is realized in the Ni@Al₂O₃/PVDF composites compared with the pristine Ni/PVDF. The enhancement can be attributed to the Al₂O₃ interlayer which not only promotes the interfacial compatibility and interactions, but also lessens the discrepancy in ϵ' and conductivity between the filler and the matrix thereby reducing the distortion and concentration of local electric field and thus frustrating the electronic transfer across the composites. The prepared Ni@Al₂O₃/PVDF composites with high ϵ' , low loss, and high E_b properties have greater potential applications in microelectronic and electrical industries.

Author contributions

All authors contributed to the study conception and design. Material preparation, data collection, and analysis were performed by WZ, YL, and PL. Characterization and related discussion were performed by TY, JL, JZ, and JC. Funding acquisition and Project administration were performed by WZ, YL. The first draft of the manuscript was written by GC and all authors commented on previous versions of the

manuscript. All authors read and approved the final manuscript.

Funding

This work was supported by the National Natural Science Foundation of China (Nos. 51937007, 51903207); Priority Research and Development Foundations of Shaanxi Provincial Government (2021GY-215); PhD Early Development Program of Xi'an University of Science and Technology (2019QDJ010), and has received research support from the Analytic Instrumentation Center of XUST.

Data availability

All data generated or analyzed during this study are included in this published article.

Declarations

Conflict of interest The authors have no relevant financial or non-financial interests to disclose. The authors have no conflicts of interest to declare that are relevant to the content of this article. All authors certify that they have no affiliations with or involvement in any organization or entity with any financial interest or non-financial interest in the subject matter or materials discussed in this manuscript. The authors have no financial or proprietary interests in any material discussed in this article. Authors are responsible for correctness of the statements provided in the manuscript. See also Authorship Principles. The Editor-in-Chief reserves the right to reject submissions that do not meet the guidelines described in this section.

References

1. Y. Feng, Y.H. Zhou, T.D. Zhang, C.H. Zhang, Y.Q. Zhang, Y. Zhang, Q.G. Chen, Q.G. Chi, *Energy Storage Mater.* **25**, 180–192 (2020)
2. B. Li, M.X. Yuan, S.H. Zhang, R. Rajagopalan, M.T. Lanagan, *Appl. Phys. Lett.* **113**(19), 193903 (2018)
3. J.W. Zha, S.C. Yao, Y. Qiu, M.H. Zheng, Z.M. Dang, *IET Nanodielectr.* **2**(3), 103–108 (2019)
4. X.G. Zhou, J.J. Yang, Z.L. Gu, Y.H. Wei, G.C. Li, C.C. Hao, Q.Q. Lei, *Adv. Eng. Mater.* **23**(7), 2100008 (2021)
5. Z.D. Wang, G.D. Meng, L.L. Wang, L.L. Tian, S.Y. Chen, G.L. Wu, B. Kong Bo, Y.H. Cheng, *Sci. Rep.* **11**(1), 1–11 (2021)
6. M.X. Yuan, G. Zhang, B. Li, T.C.M. Chung, R. Rajagopalan, M.T. Lanagan, *A.C.S. Appl. Mater. Interfaces* **12**(12), 14154–14164 (2020)
7. P. Wang, X.M. Zhang, W. Duan, W. Teng, Y.B. Liu, Q. Xie, *Chin. J. Chem.* **39**(5), 1153–1158 (2021)
8. L.H. Zhao, C.J. Liao, Y. Liu, X.L. Huang, W.J. Ning, Z. Wang, L.C. Jia, J.W. Ren, *Compos. Interface* **14**, 1–17 (2021)
9. L.H. Zhao, L. Yan, C.G. Wei, Q.H. Li, X.L. Huang, Z.L. Wang, M.L. Fu, J.W. Ren, *J. Phys. Chem. C* **124**(23), 12723–12733 (2020)
10. W.M. Xia, J.H. Zhou, T.L. Hu, P.G. Ren, G.J. Zhu, Y.L. Yin, J.L. Li, Z.C. Zhang, *Composites A* **131**, 105805 (2020)
11. B.H. Fan, X.X. Lu, Z.M. Dang, Y. Deng, X.Y. Zhou, D.L. He, J.B. Bai, *J. Appl. Polym. Sci.* **135**(3), 45693 (2018)
12. X.W. Liang, X.C. Yu, L. Lv, T. Zhao, S.B. Luo, S.H. Yu, R. Sun, C.-P. Wong, P.L. Zhu, *Nano Energy* **68**, 104351 (2020)
13. Y. Yang, H.L. Sun, D. Yin, Z.H. Lu, J.H. Wei, R. Xiong, J. Shi, Z.Y. Wang, Z.Y. Liu, Q.Q. Lei, *J. Mater. Chem. A* **3**(9), 4916–4921 (2015)
14. L.M. Yao, Z.B. Pan, J.W. Zha, G.Z. Zhang, Z.Y. Liu, Y.H. Liu, *Composites A* **109**, 48–54 (2018)
15. L.C. Jia, Y.F. Jin, J.W. Ren, L.H. Zhao, D.X. Yan, Z.M. Li, *J. Mater. Chem. C* **9**(8), 2904–2911 (2021)
16. Z.D. Wang, X.Z. Wang, S.L. Wang, J.Y. He, T. Zhang, J. Wang, G.L. Wu, *Nanomaterials* **11**(8), 1898 (2021)
17. M. Yuan, B. Li, S. Zhang, R. Rajagopalan, M.T. Lanagan, *A.C.S. Appl. Polym. Mater.* **2**(3), 1356–1368 (2020)
18. H. Luo, X.F. Zhou, C. Ellingford, Y. Zhang, S. Chen, H.C. Zhou, D. Zhang, C.R. Bowen, C.Y. Wan, *Chem. Soc. Rev.* **48**(16), 4424–4465 (2019)
19. J.W. Ren, Q.H. Li, L. Yan, L.H. Jia, X.H. Huang, L.H. Zhao, Q.H. Ran, M.L. Fu, *Mater. Des.* **191**, 108663 (2020)
20. B. Li, F. Salcedo-Galan, P.I. Xidas, E. Manias, *ACS Appl. Nanomater.* **1**(9), 4401–4407 (2018)
21. B. Li, P.I. Xidas, E. Manias, *ACS Appl. Nanomater.* **1**(7), 3520–3530 (2018)
22. B. Li, P.I. Xidas, K.S. Triantafyllidis, E. Manias, *Appl. Phys. Lett.* **111**(8), 082906 (2017)
23. O.P. Kum, N. Chanlekb, B. Putasaengc, P. Thongbaia, *Ceram. Int.* **46**(11), 17272–17279 (2020)
24. T. Li, W.Y. Zhou, Y. Li, D. Cao, Y. Wang, G.Z. Cao, X.R. Liu, H.W. Cai, Z.M. Dang, *J. Mater. Sci. Mater. Electron.* **32**, 4076–4089 (2021)
25. W.Y. Zhou, L.N. Dong, X.Z. Sui, Z.J. Wang, J. Zuo, H.W. Cai, Q.G. Chen, *J. Polym. Res.* **23**(3), 45 (2016)

26. F. Zhang, W.Y. Zhou, C.H. Zhang, Y. Li, C. Liang, X. Li, G.H. Wang, H.W. Cai, Z.M. Dang, *Polym. Plast. Technol. Mater.* **60**(6), 680–693 (2021)
27. X. Lu, W. Deng, J.D. Wei, Y.S. Zhu, P.R. Ren, Y.H. Wan, F.X. Yan, L. Jin, L. Zhang, Z.Y. Cheng, *J. Mater. Sci.* **56**(36), 19983–19998 (2021)
28. H. Luo, C. Ma, X.F. Zhou, S. Chen, D. Zhang, *Macromolecules* **50**(13), 5132–5137 (2017)
29. X. Lu, X.W. Zou, J.L. Shen, L. Zhang, L. Jin, Z.Y. Cheng, *Nano Energy* **70**, 104551 (2020)
30. X. Lu, L. Zhang, Y. Tong, Z.Y. Cheng, *Composites B* **168**, 34–43 (2019)
31. J.Y. Pei, S.L. Zhong, Y. Zhao, L.J. Yin, Q.K. Feng, L. Huang, Y.X. Zhang, Z.M. Dang, *Energy Environ. Sci.* **14**(6), 5513–5522 (2021)
32. Y.J. Kou, W.Y. Zhou, X. Li, Z.J. Wang, Y. Li, H.W. Cai, D.F. Liu, F.X. Chen, G.H. Wang, Z.M. Dang, *Polym. Plast. Technol. Mater.* **59**(6), 592–605 (2020)
33. W.Y. Zhou, Y. Gong, L.Y. Tu, L. Xu, W. Zhao, J.T. Cai, Y.T. Zhang, A.N. Zhou, *J. Alloys Compd.* **693**, 1–8 (2017)
34. W.Y. Zhou, Y.J. Kou, M.X. Yuan, B. Li, H.W. Cai, Z. Li, F.X. Chen, X.R. Liu, G.H. Wang, Q.G. Chen, Z.M. Dang, *Compos. Sci. Technol.* **181**, 107686 (2019)
35. W.Y. Zhou, F. Zhang, M.X. Yuan, B. Li, J.D. Peng, Y.Q. Lv, H.W. Cai, X.R. Liu, Q.G. Chen, Z.M. Dang, *J. Mater. Sci. Mater. Electron.* **30**(20), 18350–18361 (2019)
36. Y. Zhang, Y. Wang, Y. Deng, M. Li, J.B. Bai, *ACS Appl. Mater. Interfaces* **4**(1), 65–68 (2012)
37. D. Cao, W.Y. Zhou, T. Li, L.T. Tu, B. Li, G.Z. Cao, Y. Wang, D.F. Liu, G.H. Wang, H.W. Cai, *J. Polym. Res.* **28**(7), 1–12 (2021)
38. H.Y. Ban, Y.Z. Fan, X. Zhao, A. Du, R.N. Ma, K.X. Chen, X.M. Cao, X. Li, *Mater. Chem. Phys.* **241**, 122376 (2020)
39. L. Xu, W.Y. Zhou, B. Li, Y.J. Kou, H.W. Cai, F.X. Chen, G.H. Wang, D.F. Liu, Z.M. Dang, *J. Elastomers Plast.* **52**(4), 304–321 (2020)
40. J.C. Ma, U. Azhar, C.Y. Zong, Y.B. Zhang, A.H. Xu, C.C. Zhai, L.Q. Zhang, S.X. Zhang, *Mater. Des.* **164**, 107556 (2019)
41. W.Y. Li, Z.Q. Song, J.M. Zhong, J. Qian, Z.Y. Tan, X.Y. Wu, H.Y. Chu, W. Nie, X.H. Ran, *J. Mater. Chem. C* **7**(33), 10371–10378 (2019)
42. Y. Wu, X.Y. Lin, X. Shen, X.Y. Sun, X. Liu, Z.Y. Wang, J.K. Kim, *Carbon* **89**, 102–112 (2015)
43. Y.B. Shen, S.B. Luo, S.H. Yu, R. Sun, C.P. Wong, *ICEPT (IEEE, 2016)*, pp. 361–364
44. W.Y. Zhou, T. Li, M.X. Yuan, B. Li, S.L. Zhong, Z. Li, X.R. Liu, J.J. Zhou, Y. Wang, H.W. Cai, Z.M. Dang, *Energy Storage Mater.* **42**, 1–11 (2021)
45. D.K. Cheng, H. Wang, B. Liu, S. Wang, Y. Li, Y.S. Xia, C.X. Xiong, *J. Appl. Polym. Sci.* **136**(39), 47991 (2019)

Publisher's Note Springer Nature remains neutral with regard to jurisdictional claims in published maps and institutional affiliations.